

Time-series estimation using transition networks on realistic, sparse flow data

Frieder Kaiser[†], Giovanni Iacobello[†], and David E. Rival

Department of Mechanical and Materials Engineering, Queen's University, Kingston, Ontario, K7L 3N6, Canada

(Received xx; revised xx; accepted xx)

Inspired by biological swimming and flying that utilises distributed haptic sensors to control complex flows, a novel data-driven approach for time-series estimation is proposed. We exploit sparse, real-time pressure sensor input, in combination with pre-trained transition networks, so as to estimate aerodynamic loads in unsteady, highly-separated flows. The transition networks contain the aerodynamic states of the system as nodes along with the underlying dynamics as edges. The method is tested on realistic (i.e. noisy) experimental data from the canonical flow around an accelerating elliptical plate ($Re = 194000$) at various fixed angles of attack. Aerodynamic loads are then estimated for angles of attack cases that were not included in the training data. The network-based approach provides accurate estimates with relative errors typically averaging less than 10%, while their performance deteriorates if the estimated cases are significantly different from the training data. Based on the present findings, transition networks provide a powerful and versatile data-driven approach for real-time signal estimation, opening new avenues for applications to complex and realistic flows.

1. Introduction

The instantaneous loads on swimmers and flyers in nature is often influenced by perturbations, such as gusts in the atmosphere or the wakes of other animals. Despite challenging boundary conditions, animals control the flow over their propulsors (i.e. wings or flippers) with ease, and even utilise unsteady flows to their advantage (Liao *et al.* 2003; Portugal *et al.* 2014). Biological sensory systems monitor the flow in real-time (see figure 1a,b) by gathering haptic feedback at multiple locations on the propulsors. By combining the sensor input with their experience, animals instantaneously estimate and control their present aerodynamic state (e.g. the aerodynamic loads, figure 1d); see e.g. Zbikowski (2004); Sterbing-D'Angelo *et al.* (2011). These insights have inspired a series of studies adapting the multi-sensor principle for control of autonomous aerial vehicles. Data-driven methods, in particular, utilise sparse pressure data to characterise the instantaneous aerodynamic state of a wing. Examples include attached flow (Wood *et al.* 2019), separated two-dimensional flows (Hou *et al.* 2019), and weakly-separated, three-dimensional flows (Le Provost *et al.* 2018). Buelle *et al.* (2020) addressed highly-separated, high Reynolds-number flows around a non-slender delta wing experiencing various gusts, by linearly mapping pressure data to aerodynamic loads. However, for very sparse data, an optimised set of linear mapping coefficients only provides accurate load estimates within a limited range of unsteady boundary conditions.

To overcome the limitations of linear mapping, a non-linear data-driven approach is proposed here for load estimates in unsteady boundary conditions, even for flows that

[†] Email address for correspondence: frieder.kaiser@queensu.ca, g.iacobello@queensu.ca

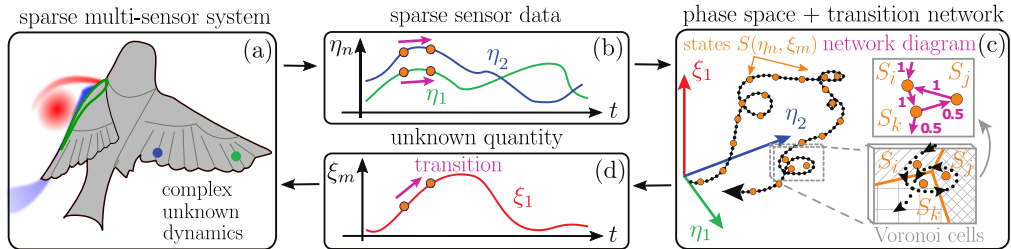


FIGURE 1. (a) Complex dynamical system with sparse sensors; (b) Exemplary sparse sensor data, η_m , collected with N sensors over time t ; (c) An example of 3D phase space (i.e., $N + M = 3$) with a trajectory (blue dotted line) and clusters centroids (orange dots). The inset shows the trajectory, displaying three different Voronoi cells associated to centroids S_i , S_j and S_k . The transition network diagram refers to the inset, where green arrows indicate the direction of transition, while numbers refer to transition probability values; (d) Estimation of M unknown signals, ξ_m , using the real-time input of sensor data and a pre-trained transition network.

are unknown *a priori*. To achieve this goal, the present work assesses the capabilities of complex networks (figure 1c) to generate new signals in real-time in the presence of input data. Complex networks have recently emerged as a versatile and powerful tool to study fluid flows as reviewed by Iacobello *et al.* (2020). In particular, transition networks, thanks to their connection with Markov models (Zou *et al.* 2019), have been successfully employed for time-series reconstruction (Shirazi *et al.* 2009; Campanharo *et al.* 2011; McCullough *et al.* 2017; Fernex *et al.* 2020), as well as for reduced-order modelling (Kaiser *et al.* 2014; Li *et al.* 2021) and control (Nair *et al.* 2019).

More specifically, in the present work we aim to perform signal estimation of M unknown signals (ξ_m , see Figure 1d) in real-time, namely to generate new signals whose specific (statistical) features can be different than those of the time-series included in the training data set. In contrast to other approaches (e.g., Fernex *et al.* 2020; Li *et al.* 2021), a testing dataset of N sparse sensors (η_m , see Figure 1b) is also exploited to guide the estimation process (§ 2), so that the estimated load signal has to agree with the measured input data. In particular, two variants of the transition-network approach are proposed that allow for signal estimation (§ 2.1 and § 2.2). The two network-based methods are tested on a simple, yet challenging, experimental test case of an accelerated elliptical plate (§ 3), captured by only two pressure sensors. The results of the load estimates are presented in § 4, showing potential as well as limitations of the two proposed methods. Finally, conclusions and future outlook for realistic and sparse data are drawn in § 5.

2. Transition networks with real-time input

In order to build transition networks, a phase space has to be defined first based on a training dataset. This is made up of N synchronised time-series from sparse sensors (figure 1b) and M signals corresponding to the variables that have to be estimated (figure 1d). An $(N + M)$ -dimensional phase space can then be obtained, where each of the $N + M$ variables corresponds to a direction, η_n or ξ_m , in the phase space with $n = 1, \dots, N$ and $m = 1, \dots, M$. By mapping series data at different times into a phase space, an oriented trajectory is formed whose direction is in increasing time. In this study, we consider only 3D phase spaces with $N = 2$ pressure signals and $M = 1$ forces (see § 3). Figure 1(c) shows a 3D phase space with an exemplary trajectory depicted as a black dotted arrow. In general, the training dataset can comprise multiple collections of $N + M$ sets of (synchronised) time-series, where each collection is referred to a different configuration parameter value, γ , referring, for instance, to different Reynolds numbers.

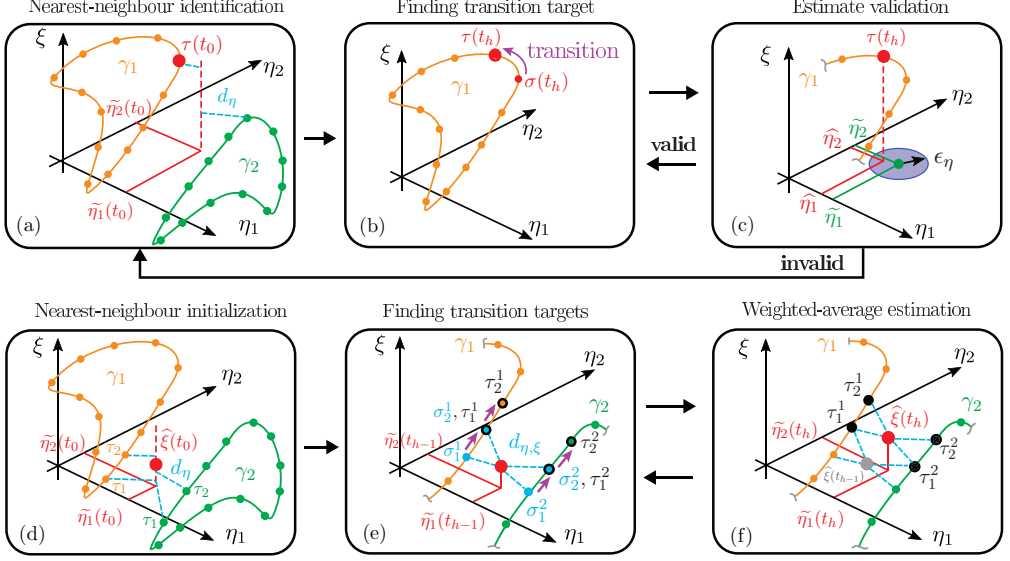


FIGURE 2. NNW method: (a) Initial estimate of state based on nearest-neighbours of initial pressure measurements; (b) Estimation using target nodes of the transition network; and (c) Validation of the predicted load with pressure data. WAB method: (d) Initial estimate of load by weighted-average using pressure input; (e) Identification of N_{nn} nearest-neighbours (source nodes) and transition targets; and (f) New estimation using targets for weighted-average.

An order reduction of the trajectories in the phase space is then performed through a clustering algorithm. Although algorithm's choice is generally problem-dependent, the underlying rationale is to rely on a spatial-proximity algorithm, since nearby points in the phase space refer to time-series values with similar intensity, thus representing a similar dynamical state. Following Fernex *et al.* (2020) and Li *et al.* (2021), the k -means algorithm, in conjunction with the k -means++ improvement (Arthur & Vassilvitskii 2006), is employed in this work to cluster trajectory points in the phase space, being a simple yet widely used technique to extract coherent clusters in an unsupervised manner (Lloyd 1982; Arthur & Vassilvitskii 2006). The k -means partitions the phase space into Voronoi cells, which are represented by cell centroids, \mathcal{S}^{γ} . In figure 1(c), cluster centroids are depicted as orange-filled circles, capturing the essential features of the black trajectory. The inset also highlights three Voronoi cells associated with three centroids (labelled as A, B and C), where orange straight lines indicate the cell edges. Although the k -means performs an unsupervised clustering, it requires an *a priori* definition of the number of clusters (i.e., centroids), N_{cl} , which should be large enough to capture the essential geometrical features of the phase space trajectories. After N_{cl} is fixed, the k -means algorithm is applied to each collection of time-series, where each collection corresponds to a configuration parameter value, γ .

Transition networks are then constructed from clustered trajectories, where cluster centroids are assigned to network nodes, while links are weighed on the probability of (temporal) transition between two nodes. The transition probability between two nodes S_i^{γ} and S_j^{γ} with $i, j = 1, \dots, N_{cl}$, is here indicated as $\mathcal{P}_{i,j}^{\gamma}$, for a given configuration γ . $\mathcal{P}_{i,j}^{\gamma}$ is computed as the fraction between (i) the number of times that trajectories directly transit from the cell of S_i^{γ} to the cell of S_j^{γ} , and (ii) the total number of times that trajectories exit from the cell of S_i^{γ} . For example, the blue trajectory in the inset of figure 1(c) uniquely transits from the cell of S_i to the cell of S_k , such that $\mathcal{P}_{i,k} = 1$

and $\mathcal{P}_{i,h} = 1 \forall h \neq k$, as reported in the transition network diagram. In general, $\mathcal{P}_{i,j}$ is not symmetric, i.e. $\mathcal{P}_{i,j} \neq \mathcal{P}_{j,i} \forall i \neq j$, so that the network is directed and links are illustrated by means of arrows indicating the direction of transition (Newman 2018). Moreover, $\sum_{j=1}^{N_{cl}} \mathcal{P}_{i,j} = 1$ and $\mathcal{P}_{i,i} = 0$ (by convention) for any $i = 1, \dots, N_{cl}$.

Transition times, $\mathcal{T}_{i,j}^\gamma$, are also defined as the average amount of time needed for transition from a node S_i^γ to a node S_j^γ (Li *et al.* 2021). As per matrix \mathcal{P} , the transition times matrix, \mathcal{T} , is also generally asymmetric ($\mathcal{T}_{i,j}^\gamma \neq \mathcal{T}_{j,i}^\gamma$).

Exploiting the features \mathcal{P} and \mathcal{T} , a new set of signals, $\{\hat{\eta}_1, \hat{\eta}_2, \hat{\xi}\}$, can be generated. Furthermore, an estimated time-vector, \hat{t} , can also be defined due to the fact that, in general, \mathcal{T} entries do not exactly correspond to the time step Δt (a consequence of the clustering operation). Although the typical approach consists in a random walk into the transition network, leading to a signal *reconstruction* (Shirazi *et al.* 2009; Campanharo *et al.* 2011; Fernex *et al.* 2020), several other strategies could be adopted. Here we present two different methods to perform signal *estimation*: transition network with nearest-neighbour validation (NNV); and weighted-average-based (WAB) transition network. In both methods, we consider the case in which N time-series values coming from a testing dataset, $\{\tilde{\eta}_1, \tilde{\eta}_2\}$, are known during the generation process of the new signals, implying that the construction of the new signal has to account for $\{\tilde{\eta}_1, \tilde{\eta}_2\}$ values.

2.1. Transition network with nearest-neighbour validation (NNV)

The NNV approach, consisting of the following three main procedural steps (see figure 2(a-c)), can be defined as follows:

(i) At the first time instance, t_0 , since the transition approach requires at least two times, a nearest-neighbour criterion is adopted to estimate $\hat{\xi}$ (as shown in figure 2a). The node, $\tau^\gamma(t_0)$ (searched among all configurations γ) with the shortest Euclidean distance, $d_\eta = \|\tilde{\boldsymbol{\eta}}(t_0) - \boldsymbol{\eta}^\gamma\|_2$, with respect to the measured pressures, $\tilde{\boldsymbol{\eta}}(t_0) = \{\tilde{\eta}_1(t_0), \tilde{\eta}_2(t_0)\}$, is identified as the most reliable for the estimation of the force at t_0 . Accordingly, the force signal is estimated as $\hat{\xi}(t_0) = \xi(\tau^\gamma(t_0))$, where this notation indicates that $\hat{\xi}(t_0)$ is equal to the ξ coordinate of the target node $\tau^\gamma(t_0)$, while $\hat{t}_0 = t_0$;

(ii) The node τ^γ at the previous time, t_{h-1} with $h \geq 1$, can then be exploited as a new source node, i.e. $\sigma^\gamma(t_h) \equiv \tau^\gamma(t_{h-1})$, and the transition probabilities can be used to perform a transition-based estimation (figure 2b). A new target node, τ^γ (shown as a larger filled red circle in figure 2b), is found following the path of maximum probability, i.e. finding the node S_j^γ that maximises $\mathcal{P}_{\sigma^\gamma, j}^\gamma$, with $j = 1, \dots, N_{cl}$. It is worth noting that the estimated signal remains constant to $\hat{\xi}(t_h) = \xi(\sigma^\gamma)$ until $\hat{t}^* \geq t_h$, where $\hat{t}^* = \hat{t}_{h-1} + \mathcal{T}_{\sigma^\gamma, \tau}^\gamma$ is the estimated time. Once the condition $\hat{t}^* \geq t_h$ is satisfied, a new target node $\tau^\gamma(t_h)$ can be identified, and the estimated force is then computed as $\hat{\xi}(t_h) = \xi(\tau^\gamma(t_h))$;

(iii) The third step of NNV consists of a validation of the target node, whether it is identified due to a network transition or during the stacked stage. The validation is done by checking that $d_\eta = \|\tilde{\boldsymbol{\eta}}(t_h) - \hat{\boldsymbol{\eta}}_i(t_h)\|_2 < \epsilon_\eta$, where ϵ_η is a threshold value (associable to the noise level of the training data, see § 4), while d_η is the Euclidean distance between the input pressure values, $\tilde{\boldsymbol{\eta}}(t_h) = \{\tilde{\eta}_1(t_h), \tilde{\eta}_2(t_h)\}$, and the values of the pressure corresponding to the current target node, $\hat{\boldsymbol{\eta}}_i(t_h) = \{\hat{\eta}_1(t_h), \hat{\eta}_2(t_h)\}$. The transition-based estimation continues as long as $d_\eta < \epsilon_\eta$ is satisfied, whereas a new node is identified through the nearest-neighbour approach as in step (i).

The validation check on step (iii) is mainly required because the transition path naturally tends to follow a given trajectory in the phase space for a specific γ . Therefore, without such a check, the estimation force tends to reconstruct a specific force included in

the training dataset (i.e., the path remains always in the same trajectory). To overcome this issue, a different strategy is adopted, as discussed in the following.

2.2. Weighted-average-based (WAB) transition network

The WAB method (see figure 2d-f) comprises three steps as per NNV, but it exploits the transition features of more than one trajectory (relative to different configuration parameters, γ) at the same time:

(i) A nearest-neighbour approach is used to calculate $\widehat{\xi}$ at $\widehat{t}_0 = t_0$ (as for NNV). Hence, a set of N_{nn} nodes, τ_i^γ with $i = 1, \dots, N_{nn}$, is selected for each configuration γ , where each set comprises the closest N_{nn} nodes to the measured pressures of the testing dataset, $\{\widetilde{\eta}_1(t_0), \widetilde{\eta}_2(t_0)\}$. For example, in figure 2(d), $N_{nn} = 2$ and the closest nodes are identified by dashed cyan lines for two configurations γ_1 and γ_2 . The force value, $\widehat{\xi}(t_0)$, is then evaluated as the weighted average of the ξ values of each node τ_i^γ , namely

$$\widehat{\xi}(t_0) = \frac{\sum_\gamma \sum_i w_i^\gamma \xi(\tau_i^\gamma)}{\sum_\gamma \sum_i w_i^\gamma}, \quad (2.1)$$

where $w_i^\gamma = 1/d_\eta$, and $d_\eta = \|\boldsymbol{\eta}(\tau_i^\gamma) - \widetilde{\boldsymbol{\eta}}(t_0)\|_2$ (see dashed cyan lines in figure 2d);

(ii) The transition features of the network are used to continue estimating the force signal. At a given time t_h , a reference node, $\{\widetilde{\eta}_1(t_{h-1}), \widetilde{\eta}_2(t_{h-1}), \widehat{\xi}(t_{h-1})\}$, is identified, whose coordinates are given by the measured pressures and the estimated force at the previous time. An example of a reference node is shown as a filled red circle in figure 2(e). N_{nn} source nodes, σ_i^γ , are selected from each trajectory (γ), identifying the first N_{nn} points that minimises the 3D Euclidean distance, $d_{\eta,\xi}$, between the reference node and the nodes belonging to each trajectory. In figure 2(e), source nodes, σ_i^γ , and the relative distances to the reference node are highlighted as cyan filled circles and dashed cyan lines, respectively. For any of these source nodes, the transition matrix is exploited to identify the target nodes, τ_i^γ , following the criterion of maximum transition probability. Target nodes are shown as black circles in figure 2(e);

(iii) A weighted average of the ξ values of target nodes is eventually used to estimate the force value at time t_h . As in step (i) of WAB method, equation (2.1) is exploited, where the weights, $w_{\eta,\xi}$, are defined as $w_{\eta,\xi} = 1/d_{\eta,\xi}$, with $d_{\eta,\xi}$ equal to the distance between the reference node and source nodes. Here, a 3D distance involving the estimated value at the previous time is used instead of a 2D distance to provide more robustness against ambiguous estimations, which arise when the η_1 and η_2 values of target and source nodes are similar while their ξ values are significantly different. The estimated time \widehat{t}_h is also computed as the sum of the previous estimated time and a $\Delta\widehat{t}$, which is obtained (similarly to load estimates) from equation (2.1), i.e. and using $w_{\eta,\xi} = 1/d_{\eta,\xi}$ and $\mathcal{T}_{\sigma,\tau}$ instead of $\xi(\tau_i^\gamma)$. In analogy with NNV, the estimated force remains constant for all times t_h of the testing dataset in between two transitions.

Note the WAB method is inspired by the procedure described by Fernex *et al.* (2020), where the weighted average is evaluated between two *a priori* configurations. Here, instead, we exploit all configurations (for any γ) of the training dataset, and the measured pressures are used as testing input data.

3. Experimental test case

As a challenging test case for the transition-network frameworks presented in §2, realistic experimental flow data were captured in a highly-separated and unsteady flow at a high Reynolds number. In particular, the canonical flow around an accelerating elliptical

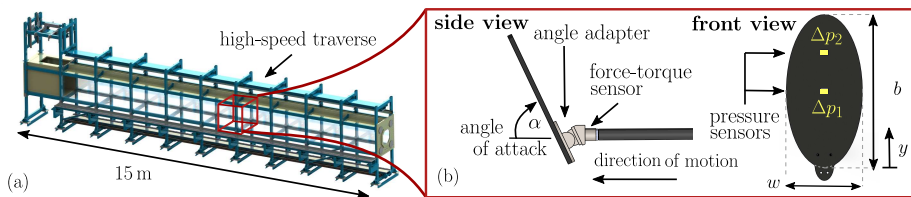


FIGURE 3. (a) Towing-tank facility; (b) front and side view of the elliptical plate model with force-torque sensor, an angle adapter to determine α and two differential pressure sensors.

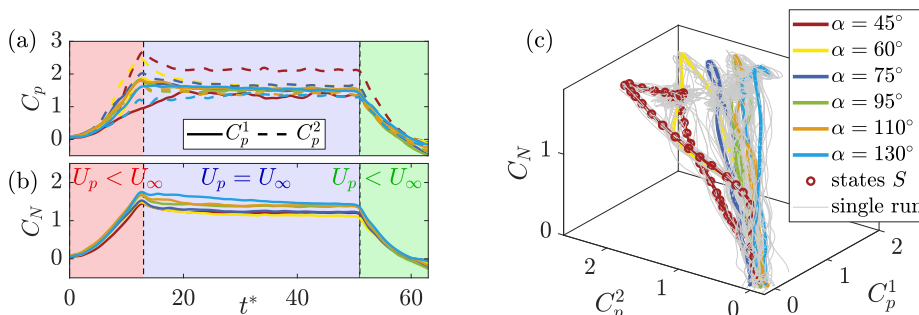


FIGURE 4. Normalised plots of (a) the differential pressures, and (b) the plate-normal force as a function of time ($t^* = U_\infty t/D_h$) for various angles of attack. The acceleration stage (red), steady stage (blue), and the deceleration stage (green) are highlighted. (c) 3D phase space built on C_N , C_p^1 , and C_p^2 . Phase-averaged data (coloured), and single-run data (grey) are both shown. For $\alpha = 45^\circ$ (red trajectory), $N_{cl} = 60$ states, S , corresponding to cluster centroids, are displayed.

plate was characterised via pressure and load measurements, and the same experimental set-up was used to obtain both training and testing datasets.

As illustrated in figure 3(a), the experiments were performed in a fully-enclosed, water-filled (viscosity ν), 15 m long towing tank facility with $1\text{ m} \times 1\text{ m}$ cross section. The model consisted of an elliptical plate with principal axes $b = 0.3\text{ m}$ and $w = 0.15\text{ m}$ and a cross-sectional area $A = \pi bw$. The model was connected to the traverse above the towing tank via a horizontal sting with diameter $0.08b$ and length $2b$, and a vertical symmetric profile of thickness $0.08b$. The plate was towed from rest with the plate velocity U_p accelerating at a rate of 0.4 m/s^2 until hitting its final velocity $U_\infty = 1\text{ m/s}$, resulting in a terminal Reynolds number of $Re = U_\infty b/\nu = 194\,000$. The plate velocity ($U_p = U_\infty$) is then kept constant over a distance of $\sim 40D_h$ before it is decelerated to rest, where D_h is the hydraulic diameter. The same kinematics were tested for the plate being mounted at various angles of attack α in the range $45^\circ < \alpha < 135^\circ$ (see figure 3b).

Two Omega differential pressure transducers capture the instantaneous differential pressure Δp between the two sides of the plate. Figure 3(b) shows the positions of the two pressure transducers at $y/b = 0.5$ (Δp_1) and $y/b = 0.75$ (Δp_2), respectively. The pressure sensors measure a range of $\pm 6895\text{ Pa}$, and have a response time of 10^{-3} s , and an accuracy of $\pm 0.25\%$ of full-scale best fit straight line (FS BFSL) with hysteresis and repeatability of 0.2% FS. In order to measure forces and moments on the plate, an ATI six-axis force-torque sensor is mounted between the plate and the horizontal sting. The transducer has a resolution of 0.125 N . Pressures and forces were recorded at a sampling frequency of 100 Hz .

Figure 4(a,b) presents the temporal evolution ($t^* = U_\infty t/D_h$) of the normalised pressures $C_p^i = 2\Delta p_i/\rho U_\infty^2$, and the plate-normal load $C_N = 2F_N/\rho A U_\infty^2$, for six angles of attack in the range $45^\circ \leq \alpha \leq 130^\circ$. Here $i = 1, 2$ refers to sensor position at

$y/b = 0.5$ and $y/b = 0.75$, respectively. The pressures and loads were phase-averaged over 10 runs, and temporally filtered with a least-squares estimator (Savitzky & Golay 1964). The standard deviation of the run-to-run pressures (averaged over all runs of all α) is $\Sigma_p = 0.05$ and is of particular interest with regard to the validation step of the NNV algorithm (see figure 2c), since Σ_p provides the order of magnitude for the acceptable error radius ϵ_η . Figure 4(c) visualises the same data in the phase space showing the single-run data (grey) in addition to the phase-averaged data (coloured). For small α , the spacing between different trajectories is notably visible while, for $\alpha > 75^\circ$, similar pressures are observed, making it difficult in this phase space to distinguish between the trajectories of different α . As such, the present dataset is particularly challenging with regard to accurate load estimates using transition networks.

4. Results and Discussion

To demonstrate the merit of the aforementioned methods suggested in § 2 on a simple example, the present section applies the transition network approaches to the experimental data described in § 3. In particular, we explore the performance of the estimation methods, when the transitional network approaches are used to estimate loads for flow configurations that are not available in the training data.

In a first step, for each configuration γ , corresponding to different angles of attack $\gamma = \alpha \in \{45^\circ, 60^\circ, 75^\circ, 95^\circ, 110^\circ, 135^\circ\}$ a transition network is built following § 2 with the pressure data ($\eta_1 = C_p^1, \eta_2 = C_p^2$) as well as the plate-normal load ($\xi = C_N$). The order of the experimental data is reduced by clustering the phase space trajectory of each α into $N_{cl} = 300$ states \mathbf{S}^α with $S_i^\alpha = \{\eta_{i,1}(\alpha), \eta_{i,2}(\alpha), \xi_i(\alpha)\}$ with $1 \leq i \leq N_{cl}$. Figure 4(c) exemplarily shows a subset of states for $\alpha = 45^\circ$. Small values of N_{cl} reduce the computational effort. However, if N_{cl} is too small, the dynamics of the trajectory in the phase space cannot be resolved. In the present study, $N_{cl} = 300$ (with 1230 time-series instants, i.e. trajectory points) provides a good balance between estimation accuracy of the load \widehat{C}_N and computational effort.

Thereafter, the transition probabilities \mathcal{P}^α , as well as the transition times \mathcal{T}^α , are obtained. Once the transition networks are established, the capabilities as well as the limitations of the suggested load-reconstruction methods (see § 2) can be tested. In particular, an estimate of the plate-normal load $\widehat{\xi} = \widehat{C}_N$ is obtained by utilising the pressure sensors' real-time input ($\widetilde{\eta}_1 = \widetilde{C}_p^1, \widetilde{\eta}_2 = \widetilde{C}_p^2$) as well as \mathcal{P}^α and \mathcal{T}^α in combination with the NNV and WAB algorithms, respectively. To test the estimation capabilities of the NNV and WAB methods, flow configurations (i.e. angles of attack, α) are used as test data that are not included in the training data. The time-series collection of one configuration (α) is excluded from the training database, and the NNV and WAB algorithms are fed with single-run data ($\widetilde{C}_p^1, \widetilde{C}_p^2$) of the omitted α . Hence, while networks are built on phase-averaged data (coloured lines in figure 4c), estimation is achieved for single runs (grey lines in figure 4c), thus accounting for single run noise.

Figure 5(a,c) shows the resulting load estimates \widehat{C}_N in comparison to the measured loads \widetilde{C}_N for different α . Figure 5(b,d) presents the relative error, $E = |\widehat{C}_N - \widetilde{C}_N|/\widetilde{C}_N$, of the estimates (\widehat{C}_N) with respect to the test data (\widetilde{C}_N). In general, the magnitude of E remains relatively small throughout the whole estimation process. However, dependent on the flow stage (acceleration, steady state, deceleration; see figure 4a,b), the estimation method (NNV, WAB), and the reconstructed configuration (α), the accuracy of the estimate varies. During the early acceleration and the late deceleration of the plate the relative error E increases. The large magnitude of E can partially be explained by the

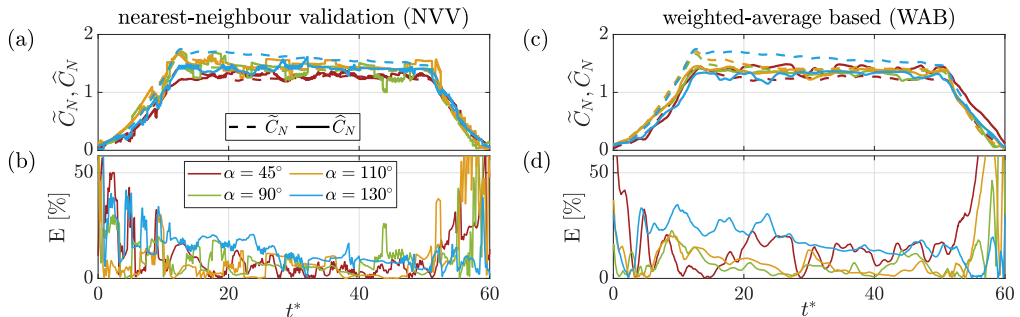


FIGURE 5. Load estimates for various α . The real-time input pressure data ($\tilde{\eta}_i = \tilde{C}_p^i$) were randomly selected among all experimental runs of the respective α . For each estimated load, the data for each respective α was not included in the training data. (a,d) Estimated loads \hat{C}_N and relative error E of the estimate using the NNV; and (b,d) estimates using the WAB method.

small signal-to-noise ratio, as well as the similar trajectories for small values of C_p^1 , C_p^2 and C_N . While for higher pressures and loads the trajectories of different α are sufficiently far apart in the phase space, and thereby enable accurate load estimates, the trajectories collapse near the phase space origin due to the presence of dense clusters of states (as shown in figure 4c). As such, the real-time input, consisting of only of two pressure signals, does not suffice to distinguish between different α for small values of \tilde{C}_p^1 and \tilde{C}_p^2 as all curves collapse within the range of the run-to-run scatter.

For the NNV method (figure 5a) the error radius is set to $\epsilon_\eta = 3\Sigma_p$. Assuming Gaussian noise, $\epsilon_\eta = 3\Sigma_p$ ensures that states are only declared invalid when they deviate further from the real-time input ($\tilde{C}_p^1, \tilde{C}_p^2$) as 99.7% of the measured data. While the NNV method performs well when reconstructing a signal that is contained in the training data (not shown here for brevity), the limitations of the NNV algorithm become apparent when a non-trained signal is estimated, as shown in figure 5(a). Throughout the whole estimation process, and for all α , a discontinuous load estimate (\hat{C}_N) is observed. Since the measured trajectory for a given α was omitted in the training data, the NNV approach tries to follow trajectories from different α . Hence, the NNV algorithm frequently detected invalid predictions, leading to re-initialisation (figure 2a) and a discontinuous load estimation.

Figure 5(c) presents load estimates obtained with the WAB approach for various α . It is apparent that the WAB approach resolves the issue of discontinuous load estimates (\hat{C}_N) observed in the NNV approach. Instead of jumping between discrete states, the WAB method constructs a novel trajectory ($\hat{C}_p^1, \hat{C}_p^2, \hat{C}_N$) in between the states (S_i) of the training data. The estimated trajectory is constructed from a weighted average at each time instance. The N_{nn} closest states S_i^α to the real-time input ($\tilde{C}_p^1, \tilde{C}_p^2$) are extracted from each collection \mathbf{S}^α of the training data, and eventually a weighted average based on the inverse 3D distance in the phase space is performed; see § 2.2. Note that Fernex *et al.* (2020), in a similar approach, used $N_{nn} < 3$ nodes for the weighted average. $N_{nn} = 10$ is selected in the present study to provide a smoother load estimate \hat{C}_N . Figure 6 emphasises the differences between NNV and WAB during the estimation process for $\alpha = 90^\circ$. For the majority of the trajectory, the measured data (green line) lies between the states of the various transition networks (gray dots). While the NNV approach (violet line) jumps in between the transition networks in the attempt to follow the pressure input, WAB (black) is able to mimic the expected trajectory reasonably well. In general, the WAB approach performs better when the trajectories of the testing data ($\tilde{C}_p^1, \tilde{C}_p^2, \tilde{C}_N$) are bounded in the phase space by training data from various configurations. For example,

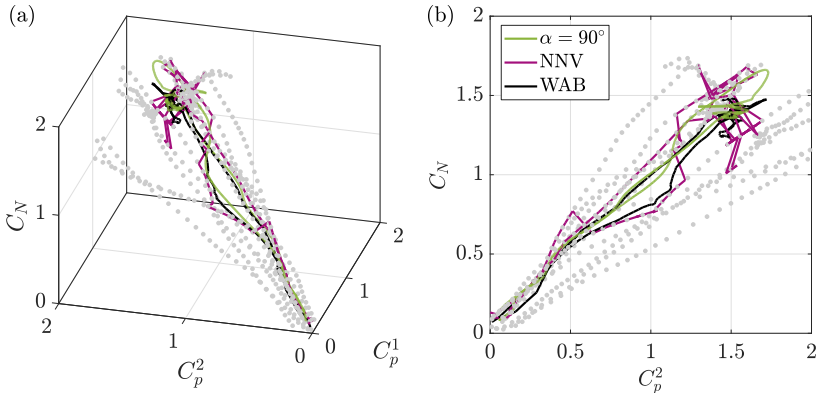


FIGURE 6. Phase space trajectory of a randomly-selected single run at $\alpha = 90^\circ$ (green) compared to estimated trajectories in the phase space. The $\alpha = 90^\circ$ data was not included in the training data set. The unknown force \hat{C}_N is estimated based on real-time input of \tilde{C}_p^1 and \tilde{C}_p^2 with the NNV (violet) and WAB (black) method, respectively. Subfigures (a,b) show different perspectives on the same visualisation. Grey dots indicate the nodes from the transition networks.

as presented in figure 6, the trajectory of $\alpha = 90^\circ$ is surrounded by states of various α . As a consequence, the weighted average leads to a decent estimate and E remains small, as presented in figure 5(d). In contrast, when estimating the load \hat{C}_N for $\alpha = 130^\circ$, only states of smaller $\alpha \leq 110^\circ$ are available in the training data. As a consequence, E is relatively large throughout the whole estimation.

5. Conclusions and Outlook

The present work represents a first step towards the application of transition networks for the estimation of time-series with realistic and sparse flow data. In particular, we suggest the extension of existing transition-network algorithms by constraining the signal estimation process, i.e. the algorithm is supplied with real-time input of a subset of variables. Two methods for the estimation of time-series data during unsteady conditions are presented. The methods exploit the features of transition networks (which comprise the definition of a phase space and a clustering algorithm), and are tested over an experimental dataset of pressure and force from an accelerating elliptical plate at various angles of attack. Transition-network-based approaches proved to be successful in generating new signals that were not included in the training dataset. Hence these tools are promising for real-time estimation of unknown variables, even under unsteady configurations.

Although the current methods happened to successfully estimate aerodynamic loads in an unsteady, high-Reynolds number flow, several methodological improvements can be implemented to advance the capabilities of our approach. In fact, additional physical insights can be included in the network model by expanding the size of the phase space, where additional axes could represent other measured variables of the system. In this regard, future efforts can incorporate external flow measurements (e.g., velocity or vorticity fields) in the transition network model, which can also rely on random-walks with or without memory (Fernex *et al.* 2020). Furthermore, with the aim to account for noise in experimental data, different clustering strategies could also be applied (such as fuzzy algorithms), as well as to further exploit the probabilistic nature of transition networks, e.g., implementing Bayesian statistics. In conclusion, transition networks do not represent a *black box* between input and output variables, but rather a versatile

method that, based on present findings, can pave the way for real-time estimation of realistic flows even when limited by sparse data.

Acknowledgements: DER acknowledges support from the Air Force Office of Scientific Research (AFOSR) under Grant No. FA9550-20-1-0086, monitored by Dr. Gregg Abate.

Declaration of interests: The authors report no conflict of interest.

REFERENCES

- ARTHUR, D. & VASSILVITSKII, S. 2006 k-means++: The advantages of careful seeding. *Tech. Rep.*. Stanford.
- BURELLE, L., YANG, W., KAISER, F. & RIVAL, D. E. 2020 Exploring the signature of distributed pressure measurements on non-slender delta wings during axial and vertical gusts. *Phys. Fluids* **32** (115110).
- CAMPANHARO, A., SIRER, M. I., MALMGREN, R. D., RAMOS, F. M. & AMARAL, L.A.N. 2011 Duality between time series and networks. *PloS one* **6** (8), e23378.
- FERNEX, D., NOACK, B. R. & SEMAAN, R. 2020 Cluster-based network modeling—automated robust modeling of complex dynamical systems. *arXiv preprint:2010.16364* .
- HOU, W, DARAKANANDA, D & ELDRIDGE, J 2019 Machine-learning-based detection of aerodynamic disturbances using surface pressure measurements. *AIAA J.* **57** (12), 5079–5093.
- IACOBELLO, G., RIDOLFI, L. & SCARSOGLIO, S. 2020 A review on turbulent and vortical flow analyses via complex networks. *Physica A* p. 125476.
- KAISER, E., NOACK, B.R., CORDIER, L., SPOHN, A., SEGOND, M., ABEL, M., DAVILLER, G., ÖSTH, J., KRAJNOVIĆ, S. & NIVEN, R.K. 2014 Cluster-based reduced-order modelling of a mixing layer. *J. Fluid Mech.* **754**, 365–414.
- LE PROVOST, M., HE, X. & WILLIAMS, D. R 2018 Real-time roll and pitching moment identification with distributed surface pressure sensors on a ucas wing. In *2018 AIAA Aerospace Sciences Meeting*, p. 0326.
- LI, H., FERNEX, D., SEMAAN, R., TAN, J., MORZYŃSKI, M. & NOACK, B. R. 2021 Cluster-based network model. *J. Fluid Mech.* **906**.
- LIAO, J.C., BEAL, D.N., LAUDER, G.V. & TRIANTAFYLLOU, M.S. 2003 Fish exploiting vortices decrease muscle activity. *Science* **302** (5650), 1566–1569.
- LLOYD, S. 1982 Least squares quantization in pcm. *IEEE T. Inform. Theory* **28** (2), 129–137.
- MCCULLOUGH, M., SAKELLARIOU, K., STEMLER, T. & SMALL, M. 2017 Regenerating time series from ordinal networks. *Chaos* **27** (3), 035814.
- NAIR, AG, YEH, C., KAISER, E., NOACK, BR, BRUNTON, SL & TAIRA, K. 2019 Cluster-based feedback control of turbulent post-stall separated flows. *J. Fluid Mech.* **875**, 345–375.
- NEWMAN, M. 2018 *Networks*. Oxford university press.
- PORTUGAL, S.J., HUBEL, T.Y., FRITZ, J., HEESE, S., TROBE, D., VOELKL, B., HAILES, S., WILSON, A. M. & USHERWOOD, J. R. 2014 Upwash exploitation and downwash avoidance by flap phasing in ibis formation flight. *Nature* **505** (7483), 399–402.
- SAVITZKY, A. & GOLAY, M. J. E. 1964 Smoothing and differentiation of data by simplified least squares procedures. *Anal. Chem.* **36**, 1627–1639.
- SHIRAZI, A.H., JAFARI, G.R., DAVOUDI, J., PEINKE, J., TABAR, M.R.R. & SAHIMI, M. 2009 Mapping stochastic processes onto complex networks. *J. Stat. Mech.* **2009** (07), P07046.
- STERBING-D’ANGELO, S., CHADHA, M., CHIU, C., FALK, B., XIAN, W., BARCELO, J., ZOOK, J. M. & MOSS, C. F. 2011 Bat wing sensors support flight control. *PNAS USA* **108** (27), 11291–11296.
- WOOD, K. T., ARAUJO-ESTRADA, S., RICHARDSON, T. & WINDSOR, S. 2019 Distributed pressure sensing-based flight control for small fixed-wing unmanned aerial systems. *Journal of Aircraft* **56** (5), 1951–1960.
- ZBIKOWSKI, R. 2004 Sensor-rich feedback control: a new paradigm for flight control inspired by insect agility. *IEEE Instru. Meas. Mag.* **7** (3), 19–26.
- ZOU, Y., DONNER, R.V., MARWAN, N., DONGES, J.F. & KURTHS, J. 2019 Complex network approaches to nonlinear time series analysis. *Phys. Rep.* **787**, 1–97.